Highly Efficient Photocathodic Protection Performance of 2D/2D ZIS@CNNs Composites under Visible Light

Weitao Li , Zhanyuan Yang , Yanhui Li , Pengfei Zhang , Hong Li *

Posted Date: 5 July 2023

doi: 10.20944/preprints202307.0233.v1

Keywords: g-C3N4; ZnIn2S4; photocathodic protection; composites; XPS

Article

Highly Efficient Photocathodic Protection Performance of 2D/2D ZIS@CNNs Composites under Visible Light

Weitao Li [1], Zhanyuan Yang [1], Yanhui Li [1,2], Pengfei Zhang [1] and Hong Li [1,*]

[1] College of Mechanical and Electrical Engineering, Qingdao University, Qingdao 266071, Shandong Province, China.

[2] State Key Laboratory of Bio-Fibers and Eco-Textiles, Qingdao University, Qingdao 266071, Shandong Province, China.

* Correspondence: lhqdio1987@163.com; Tel.: +86-532-85953679.

Abstract: Low separation efficiency of photogenerated carriers and inefficient utilization of visible light limit the application of g-C_3N_4 nanosheets (CNNs) in the field of photocathodic protection (PCP). Therefore, this work considered indium zinc sulfide ($ZnIn_2S_4$, ZIS) as a visible photosensitizer and an electronic donor to promote its PCP performance. ZIS nanolayers with nano-leaf structures were fabricated on CNNs by a simple hydrothermal method. The synthesized 30% ZIS@CNNs composites significantly enhanced the PCP performance for 316 stainless steel (SS) compared with pure CNNs. Under visible light illumination, the 30% ZIS@CNNs photoelectrode exhibited the largest photoinduced current density of 17.30 μA cm^{-2} and a photoinduced potential drop of 0.37 V, which was approximately 4 and 7.5 times higher than that of pure CNNs, respectively. The improved protection performance may be attributed to the significant increase in visible light absorption and the great enhancement in the separation efficiency of photoinduced electrons and holes.

Keywords: g-C_3N_4; $ZnIn_2S_4$; photocathodic protection; composites; XPS

1. Introduction

Photocathodic protection (PCP) technology has attracted extensive attention because it is a promising green and clean technology in the past decades [1–4]. This technology takes the advantage of photosensitive characteristics of semiconductor photoanode materials to generate electrons under light with a certain energy level and protects metals from corrosion by transferring electrons to the metal surface and causing a negative shift of the metal's potential.

As a metal-free semiconductor, g-C_3N_4 (~2.7 eV) is widely applied in many fields such as photocatalytic hydrogen production [5–7], degradation of organic pollutants [8–10], and CO_2 reduction, etc. [11,12] due to the advantages of visible light response, obvious chemical stability, easy preparation, rich reserves, and strong environmental affinity. Compared with metal-semiconductor, g-C_3N_4 has incomparable advantages in avoiding secondary pollution [13]. However, the protection of metals by g-C_3N_4 materials may not be ideal due to its low surface area, rapid recombination of photogenerated electron-hole pairs, and inefficient utilization of visible light [14–17]. In order to address these issues, various approaches, including nanostructure design [18,19], elemental doping [20,21], and heterojunction construction [22,23], have been applied to modify g-C_3N_4. Among these strategies, heterojunction construction is recognized as one of the most effective approaches to suppress the carrier recombination and improve the absorption efficiency of visible light, such as $NaNbO_3$/g-C_3N_4 [24], $KBiFe_2O_5$/g-C_3N_4 [25], Co_3O_4/g-C_3N_4 heterojunction [26].

As a unique ternary sulfide n-type semiconductor, $ZnIn_2S_4$ (ZIS, 2.34 ~ 2.55 eV) has been widely used in the photocatalytic fields due to its exceptional layered structure, tunable band gap, and excellent visible light absorption properties [27–29]. Compared with conventional binary metal sulfides, ZIS has higher photo-corrosion resistance and better chemical stability, which has aroused

 doi:10.20944/preprints202307.0233.v1

great attention of researchers in the field of PCP [30]. However, ZIS still has some limitations in its applications, including poor photoelectron mobility and low carrier separation efficiency [31–33]. Coupling g-C_3N_4 with ZIS to construct heterojunction composites is an effective method to enhance their photocatalytic performance under visible light. For example, Dang et al. reported that g-C_3N_4/ZIS composite showed better photocatalytic hydrogen production activity than pure ZIS and g-C_3N_4 [34]. Hou et al. reported that g-C_3N_4/ZIS composite exhibited good photocatalytic degradation of ofloxacin performance and higher photocatalytic hydrogen evolution than pure g-C_3N_4 and ZIS [35]. However, no application of g-C_3N_4/ZIS composites in the field of PCP has been reported.

The morphological structure and size of semiconductors play an important role in the process of photogenerated electron-hole pairs. The ultrathin two-dimensional (2D) g-C_3N_4 nanosheets (CNNs) are regarded as an ideal structure that can significantly enlarge the specific surface area, shorten the transfer distance of photoelectrons, and expose a considerable number of active sites, thus effectively improving the performance of g-C_3N_4 [36,37]. In addition, it has been reported that the 2D/2D morphology in the heterojunction composites can significantly facilitate electron migration and boost visible light absorption ability [38], which may improve the utilization efficiency of photogenerated carriers and enhance the PCP performance under visible light.

In this work, we fabricated the 2D/2D ZIS@CNNs composites by two-step calcination and hydrothermal method and then coated the composites onto the fluorine-doped tin oxide (FTO) substrates. The microstructures, chemical compositions, and crystalline structures of the composites were identified by scanning electron microscope (SEM), transmission electron microscopy (TEM), X-ray photoelectron spectroscopy (XPS), and X-ray diffraction (XRD). The optical absorption properties were investigated using UV-Vis diffuse reflectance spectroscopy (DRS). The separation efficiency of photogenerated carriers was investigated by PL spectroscopy. The PCP performances of the composites were evaluated by photoinduced open circuit potential (OCP) and photocurrent densities. The PCP mechanism was proposed by analyses of electrochemical impedance spectroscopy (EIS) and Mott-Schottky (M-S) curves.

2. Experimental

2.1. Materials

Chemicals: melamine ($C_3N_3(NH_2)_3$)), zinc nitrate hexahydrate ($Zn(NO_3)_2{\cdot}6H_2O$), thioacetamide (TAA), indium nitrate tetrahydrate ($In(NO_3)_3{\cdot}4H_2O$), sodium citrate dihydrate ($C_6H_5O_7Na_3{\cdot}2H_2O$) were all purchased from Sinopharm Chemical Reagent Co. Ltd (Shanghai, China). All reagents are analytically pure.

FTO glasses (7 Ω cm^{-2}, 10 × 20 × 2.2 mm) were purchased from Guluo Glass Co. Ltd, (Luoyang, China). The glasses were ultrasonically cleaned in deionized water, acetone, and anhydrous ethanol for 30 min in sequence. Then these substrates were dried naturally at room temperature.

2.2. Synthesis of CNNs

CNNs were fabricated by a two-step calcination method (Figure 1). First, 5 g melamine was calcined at 520 ℃ for 4 h with a heating rate of 5 ℃·min^{-1} in a tube furnace. Afterward, the resultant sample was kept calcining (heating rate: 2.5 ℃/min) at 550 ℃ for 2 h. The light yellow CNNs were collected (Figure S1).

 doi:10.20944/preprints202307.0233.v1

Figure 1. Schematic diagram of the preparation of ZIS@CNNs composites.

ZIS nano-leaves were fabricated onto CNNs by a simple hydrothermal method. Firstly, precursor solutions were obtained by adding 0.1 mmol $Zn(NO_3)_2 \cdot 6H_2O$, 0.2 mmol $In(NO_3)_3 \cdot 4H_2O$, and 0.6 mmol sodium citrate dihydrate to the beaker filled with 20 mL deionized water and stirring vigorously for 0.5 h at room temperature. Secondly, different weights of CNNs were added into the precursor solution. The above solution was first treated by ultrasonication for 10 min and then stirred for 3 h to obtain a white suspension. Finally, 0.8 mmol TAA was added to the above suspension, sonicated for 10 min, and churned for 30 min. Then, the above solution was poured into a 30 mL Teflon-lined stainless-steel autoclave, and heated in an oven at 160 °C for 1 h. After cooling down, it was washed with deionized water and anhydrous ethanol, respectively, then collected by centrifugation and dried at 60 °C for 24 h. ZIS@CNNs composites (Figure S1) with different proportions of ZIS were obtained and marked as 20% ZIS@CNNs, 30% ZIS@CNNs, and 40% ZIS@CNNs composites, respectively. As a reference, pure ZIS nano-leaves were also synthesized under similar conditions without CNNs.

2.3. Fabrication of ZIS@CNNs photoelectrodes

The treated FTO was sealed with tape, and only a 10 × 15 mm conductive surface was left as the working surface. 20 mg ZIS@CNNs composite was added to a mixed solution containing 10 μL naphthol and 1 mL anhydrous ethanol, and sonicated for 15 min. A uniform suspension was obtained. 40 μL of the above solution was applied drop by drop to the conductive surface of the FTO, so that the suspension was distributed as uniformly as possible on the surface of the FTO (about 0.528 mg cm^{-2}). Then the FTO was dried in the air atmosphere and transferred into an oven to heat at 100 ℃ for 2 h to obtain ZIS@CNNs photoelectrodes.

2.4. Characterization

The crystal structures of CNNs, ZIS, and ZIS@CNNs were detected by XRD diffractometer (Rigaku Ultima IV) with Cu Kα radiation. The elemental compositions and bonding information of the synthetic products were analyzed using XPS (Thermo ESCALAB 250XI Al Kα as the X-rays). The microstructure and chemical composition of the composite were identified using a high-resolution transmission electron microscope (HRTEM, JEM 200CX TEM). UV-Vis diffuse reflectance spectrometer (Shimadzu UV-3600i Plus, Japan), was used to measure the absorption capacity of materials using $BaSO_4$ plates used as a reference. Photoluminescence (PL, FLS-980) was used to measure the photogenerated carrier separation efficiency of materials, with an excitation wavelength of 320 nm. The fourier transform infrared spectroscopy (FT-IR, Thermo Scientific Nicolet iS20, America) was tested at the wavelength range of 400 ~ 4000 cm^{-1}.

2.5. Electrochemical tests

An electrochemical workstation (CHI760E, Chenhua Instrument Co., Ltd., Shanghai, China) was used to test the electrochemical properties of the fabricated photoelectrodes. The H-type electrochemical cell was selected for electrochemical performance testing, which was filled with a 3.5 wt% NaCl solution and a mixture solution of 0.1 M Na_2S and 0.2 M NaOH in the corrosion chamber and photochemical chamber, respectively. Conductivity between electrolyte solutions in two electrolytic cells was performed through the Nafion membrane (N-117, DuPont Co., America). The ZIS@CNNs photoanode was placed in the photochemical chamber, whereas the 316 stainless steel (SS) electrode with an active area of 1 cm^2 was placed in the corrosion chamber as the test subject. A 300W Xe lamp (PLS-SXE300, Perfect-light Co., Ltd., Beijing, China) was used to be the light source (Figure S2a). The light illuminated on the photoelectrode through a quartz window with a diameter of 30 mm on the side of the photochemical chamber. A 420 nm filter was used to filter out light below 420 nm. During the measurements of OCP, EIS, and Tafel, the photoanode and 316 SS were connected by wires as working electrode (WE). The saturated calomel electrode (SCE) and Pt sheet were regarded as reference electrode (RE) and counter electrode (CE), respectively. The EIS tests were

Preprints (www.preprints.org) | NOT PEER-REVIEWED | Posted: 5 July 2023 doi:10.20944/preprints202307.0233.v1

conducted under light and performed at a frequency range of 10^{-2} ~ 10^{5} Hz, with an alternating current amplitude of 5 mV. The Tafel test was conducted under light and performed at range of −0.25 ~ 0.25 V (vs. OCP). During the measurement of photocurrent densities, the photoanode and 316 SS were connected to WE and ground electrode, respectively, and RE and CE were connected in a short circuit (Figure S2b). The M-S tests were conducted under the light and measured with a frequency of 1000 Hz. A conventional three-electrode system was used for this testing with 0.1 mol L^{-1} Na_2SO_4 solution as the electrolyte solution. The photoelectrode, SCE, and Pt sheet were taken as the WE, RE, and CE, respectively.

3. Results and discussion

3.1. Characterization of ZIS@CNNs composites

Figure 2a-c showed the morphological images of CNNs, ZIS, and ZIS@CNNs composites, respectively. It could be observed from Figure 2a that pure CNNs prepared via two-step calcination method had distinct flaky images and exhibited overlapping and stacking morphologies. As can be seen from Figure 2b that the morphology of pure ZIS synthesized by the hydrothermal method resembles nano-leaves. As shown in Figure 2c, the bottom layer of the ZIS@CNNs composite material is CNNs, and ZIS nano-leaves are evenly attached to its surface. These results indicate that ZIS nano-leaves are successfully grown on CNNs. Figure 2d shows the chemical composition of the ZIS@CNNs composites obtained by EDS testing, which shows the presence of Zn, In, S, C, and N elements.

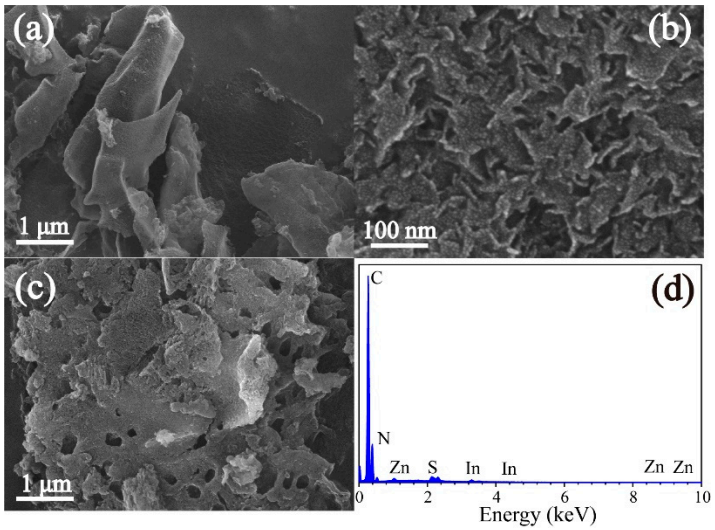

Figure 2. SEM image of (a) CNNs, (b) ZIS, (c) 30% ZIS@CNNs; (d) EDS spectrum, and (e) EDS mappings of 30% ZIS@CNNs composite.

When CNNs were added to the ZIS precursor solution with dissolved sodium citrate dihydrate, Zn^{2+} and In^{3+} in the solution moved rapidly to CNNs, and then the added TAA released S^{2-}, which reacted with Zn^{2+} and In^{3} attached to the surface to form ZIS nanoparticles. Under hydrothermal conditions, sodium citrate dihydrate exerted an inhibitory effect on the growth of nanoparticles, and then the nanoparticles gradually became nano-leaves. Eventually, a large number of ZIS nano-leaves accumulated on the surface of CNNs, forming 2D/2D ZIS@CNNs heterojunctions.

The microscopic morphologies of CNNs, ZIS, and 30% ZIS@CNNs were further investigated using TEM. From Figure 3a and b, it was clear that the morphologies of CNNs and ZIS were nanosheets and nano-leaves, respectively. The surface of the 30% ZIS@CNNs composite is rougher than that of pure CNNs due to the deposition of the ZIS nano-leaves onto the surface of the CNNs, which is consistent with the SEM results. Figure 3d displayed the HRTEM image of 30% ZIS@CNNs. The lattice spacing of 0.321 nm corresponds to the (002) crystalline planes of CNNs, and the lattice spacing of 0.315 nm corresponds to the (104) crystalline planes of ZIS (JCPDS No. 49−1562).

Preprints (www.preprints.org) | NOT PEER-REVIEWED | Posted: 5 July 2023 doi:10.20944/preprints202307.0233.v1

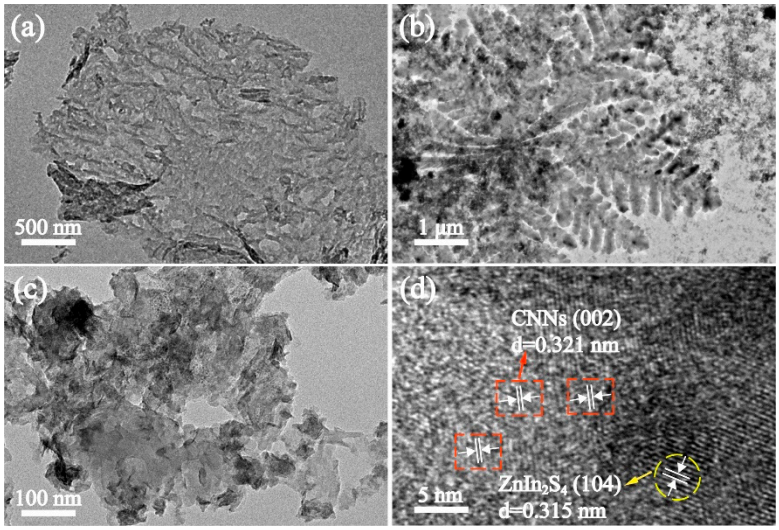

Figure 3. TEM image of (a) CNNs, (b) ZIS, (c) 30% ZIS@CNNs. HRTEM images of (d) 30% ZIS@CNNs composite.

Figure 4a,b shown the N_2 adsorption–desorption isotherms and pore size distribution curves of CNNs and 30% ZIS@CNNs composite, respectively. According to the adsorption isotherm, the S_{BET} of CNNs was 656.965 m^2/g, while the S_{BET} of 30% ZIS@CNNs composite decreased sharply to 47.239 m^2/g. The pore size distribution of 30% ZIS@CNNs composite and CNNs were analyzed according to the Barrett-Joyner-Halenda (BJH) method [39], The average pore diameters of 30% ZIS@CNNs composite and CNNs are about 13.05 and 4.38 nm, respectively, indicating that both materials are mesoporous structures.

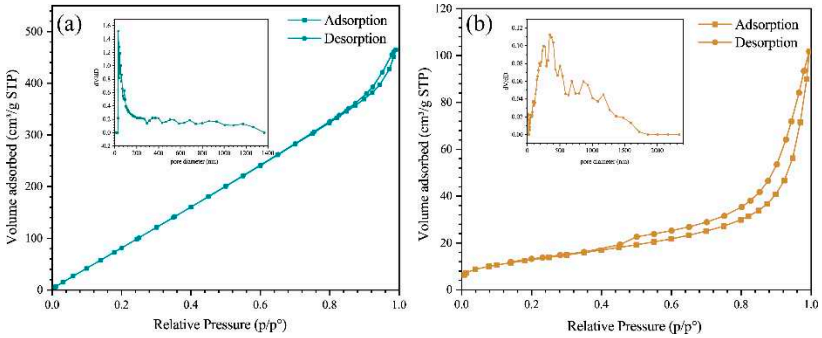

Figure 4. N_2 adsorption–desorption isotherms and pore size distribution curves of (a) CNNs and (b) 30% ZIS@CNNs composite.

Figure 5a displayed the XRD patterns of pure CNNs, pure ZIS, and three different ZIS@CNNs composites. It could be obviously seen from Figure 5a that there were two evident characteristic peaks in the XRD patterns of CNNs. The weak peak at 12.9° can be assigned to an in-plane repeating motif of the continuous heptazine network [40,41]. Due to the interlayer-stacking (002) crystal plane of melon networks, there is a prominent and sharp diffraction peak at 27.7° [42]. From the XRD patterns of ZIS, the peak at 28.3°, 47.0°, and 55.8° can be assigned to the diffraction peaks of (104), (110), and (024) hexagonal crystal planes of ZIS (JCPDS No. 49−1562), respectively. For the three different ZIS@CNNs composites, the peak of (002) crystal plane of CNNs overlaps with the peak of (104) hexagonal crystal plane of ZIS, and the remaining two peaks are the characteristic diffraction peaks of ZIS. In addition, due to the introduction of ZIS, the diffraction peak density of CNNs is weakened. However, the peak position of CNNs does not move, indicating that the introduction of ZIS does not change the crystal phase structure of CNNs.

Preprints (www.preprints.org) | NOT PEER-REVIEWED | Posted: 5 July 2023 doi:10.20944/preprints202307.0233.v1

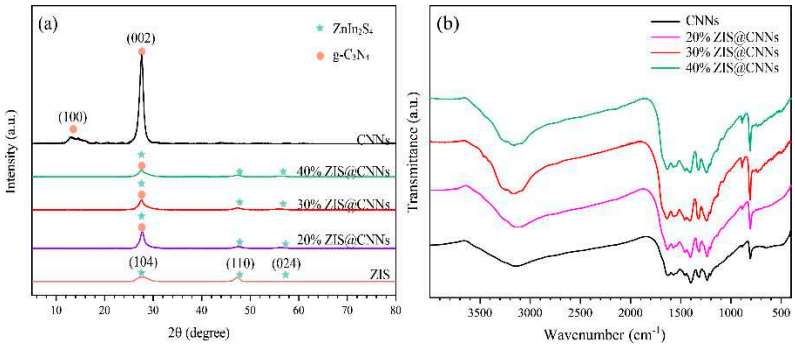

Figure 5. (a) The XRD patterns (b) FT-IR spectrum of CNNs and three different ZIS@CNNs composites.

FT-IR spectra were used to characterize the variation of CNNs in the reaction process. As displayed in Figure 5b, several strong peaks appeared in the region of 900–1700 cm^{-1} are caused by the skeleton vibration of C-N and C=N heterocycles [43]. And the peak located at 808 cm^{-1} is caused by the breathing vibration of the s-triazine units [44]. The peaks between 3000 and 3500 cm^{-1} are caused by H_2O molecules bound with surfaces of CNNs and ZIS@CNNs and the amino groups formed by the hydrothermal reaction [45]. Compared with the FT-IR spectra of CNNs and three different ZIS@CNNs composites, the peaks of the four curves were similar, which indicates that the introduction of ZIS does not damage the skeleton structure of CNNs. ZIS and CNNs can co-exist well in the hydrothermal reaction. It also shows that CNNs have excellent structural stability.

XPS was considered as an effective means to further study the surface chemical state of the ZIS@CNNs composites. As could be seen in Figure 6a, five elements, Zn, In, N, S, and C, were clearly present in the tested material. Figure 6b shown the high-resolution XPS spectrum of element C. It could be clearly seen that the peaks of CNNs and ZIS@CNNs composites were very similar, which indicates the presence of CNNs in the composites. The strong peak locates at 287.6 eV is assigned to N–C=N and the weaker peak at 284.3 eV is assigned to graphite carbon nitride [46]. The peak of ZIS@CNNs composites negatively shift to 287.5 and 284.2 eV, respectively. The binding energy of ZIS@CNNs composites decreases by 0.1 eV compared to CNNs. This may be attributed to the intense electronic interactions between CNNs and ZIS, where CNNs gain photoelectrons [47]. Figure 6c shown the high-resolution XPS spectrum of element N. Four peaks can be seen in Figure 6c, and the intensity of these four peaks gradually decreased from 398.0 to 403.7 eV. The peak with the highest binding energy at 398.0 eV is caused by the C–N=C bond. The peak at 399.6 eV is caused by $N–(C)_3$ groups. The peak at 400.5 eV indicates the presence of N–H bonds [48]. The weak peak at 403.7 eV is caused by charge buildup due to electron transfer. In comparison with CNNs, the binding energy of element C, N of the ZIS@CNNs composites negatively shift, indicating the state of CNNs gaining photoelectrons. To further analyze the electronic state of ZIS, high-resolution XPS spectra of Zn, In, and S elements were analyzed. It can be seen that the peaks of ZIS and ZIS@CNNs composites are very similar, which indicates the presence of ZIS in the composites. Figure 6d shows the high-resolution XPS spectrum of element S. It could be seen two peaks with different peak widths. The narrow peak at 160.6 eV is the characteristic peak of S $2p_{3/2}$ and the broad peak at 161.8 eV is the characteristic peak of S $2p_{1/2}$, indicating the S^{2-} chemical state in the ZIS@CNNs composite. Figure 6e shows the high-resolution XPS spectrum of element In, the peaks at 444.2 and 451.6 eV are the characteristic peaks of In $3d_{5/2}$ and In $3d_{3/2}$, respectively, indicating the In^{3+} chemical state in ZIS@CNNs composite [49]. As displayed in Figure 6f, the peaks at 1021.3 and 1044.8 eV are the characteristic peaks of Zn $2p_{3/2}$ and Zn $2p_{1/2}$, respectively, indicating the Zn^{2+} chemical state in ZIS@CNNs composite [50]. In comparison with ZIS, the binding energy of element S, In, Zn of the ZIS@CNNs composites positively shift, indicating the state of ZIS losing photoelectrons [51]. Combining the above results of the gain and loss of photoelectrons in CNNs and ZIS, it can be judged that photoelectrons flow from ZIS to CNNs.

Preprints (www.preprints.org) | NOT PEER-REVIEWED | Posted: 5 July 2023 doi:10.20944/preprints202307.0233.v1

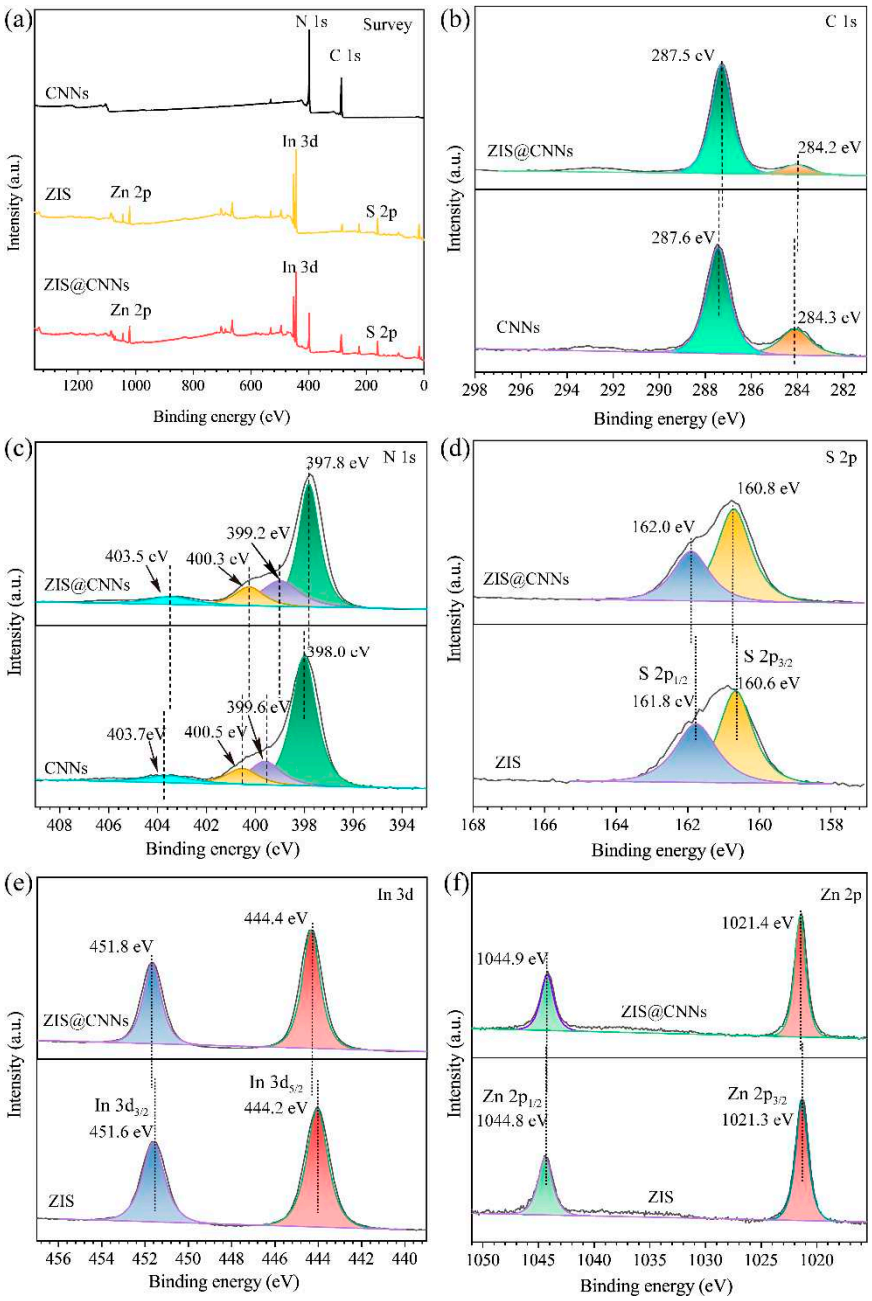

Figure 6. Full scan survey XPS spectra and high-resolution XPS spectra of (b) C 1s, (c) N 1s, (d) Zn 2p, (e) In 3d and (f) S 2p from CNNs, ZIS, and 30% ZIS@CNNs composite.

3.2. Light absorption properties

To investigate the absorption properties of CNNs and three different composites for visible light, their UV-Vis DRS was measured [52]. It can be clearly seen from Figure 7a that the absorption edges of the three different ZIS@CNNs composites are significantly red-shifted toward the visible region compared with pure CNNs, and the 30% ZIS@CNNs composite shows the largest absorption threshold, which indicates that the ZIS@CNNs composites have stronger absorption of visible light than pure CNNs, and the 30% ZIS@CNNs composite has the best absorption performance. From the results of TEM and SEM as well as BET, it is obvious that the introduction of ZIS makes the CNNs porous structures as well as the increased area of visible light contact, which allows more visible light to be captured through the pores into the gaps between the CNNs, thus the composites exhibit a strong light capture capability. In addition, the Tauc curves (Figure 7b) are obtained by Kubelka–Munk means [53,54]:

Preprints (www.preprints.org) | NOT PEER-REVIEWED | Posted: 5 July 2023 doi:10.20944/preprints202307.0233.v1

$$(\alpha hv) = A(hv - E_g)^n \quad (1)$$

where the absorption index, the Planck constant, the frequency, and the characteristic constant are defined as α, h, v, and A, respectively. The value of n depends on the transition characteristics of the material, n = 1/2 for the direct band gap and n = 2 for the indirect band gap. The E_g of pure CNNs, ZIS, 20% ZIS@CNNs, 30% ZIS@CNNs, and 40% ZIS@CNNs composites are 2.7, 2.39, 2.63, 2.52, and 2.59 eV, respectively.

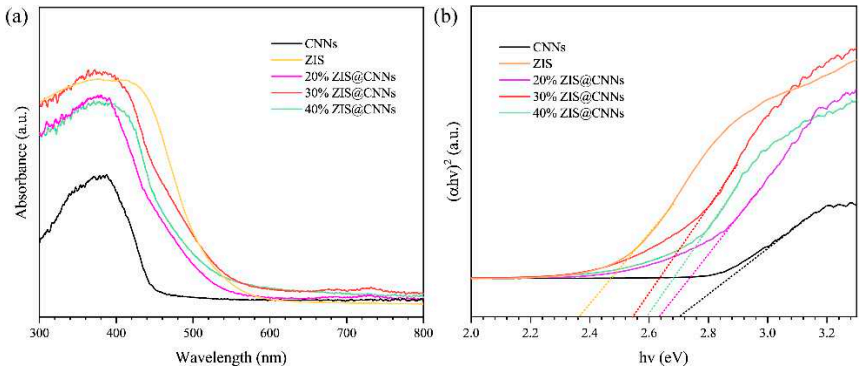

Figure 7. (a) UV−Vis DRS, (b) plot of $(\alpha h\nu)^2$ versus hν for the band gap energy of CNNs, and ZIS@CNNs composites with different ZIS content.

The separation efficiency of photogenerated carriers has an important influence on the PCP performance of the material. In order to study the carrier separation efficiency of different materials [55], PL tests were performed which can be seen in Figure 8. The greater the decay of PL peak intensity, the higher the carrier separation efficiency [56]. Compared with pure CNNs, the peak intensities of the three different ratios of composites decayed significantly, with the 30% ZIS@CNNs composite showing the greatest decay. This may be due to the introduction of ZIS, which makes the ZIS@CNNs composites exhibit significant fluorescence quenching. The above results indicate that the recombination efficiency of the photogenerated electron-hole pairs of the composites is significantly reduced, and the 30% ZIS@CNNs composite has the lowest carrier recombination efficiency.

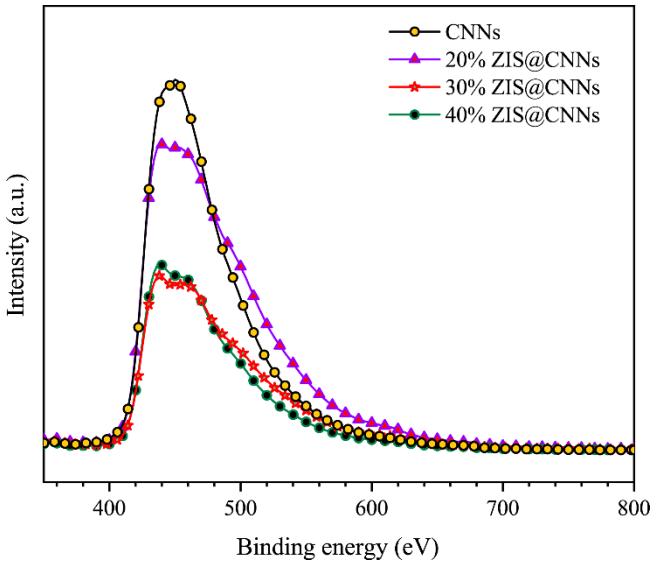

Figure 8. Steady-state PL spectra of CNNs, and ZIS@CNNs composites with different ZIS content.

3.3. PCP effects

In order to test the protection effect of CNNs and three different ZIS@CNNs composites on 316 SS, we conducted OCP tests on the above four materials [57]. As can be seen in Figure 9a, the OCP of all materials dropped steeply as the light source was turned on, and the potential drops of three

Preprints (www.preprints.org) | NOT PEER-REVIEWED | Posted: 5 July 2023 doi:10.20944/preprints202307.0233.v1

different ZIS@CNNs composites were significantly higher than that of pure CNNs. In addition, 30% ZIS@CNNs exhibited the largest potential drop (0.37 V), which was 7.4 times higher than that of pure CNNs (0.05 V). After the power was turned off, the OCP first rosed sharply and then slowly and finally stabilized around a certain value. As could be seen from Figure 9a, the stable values of the rebound potentials of both ZIS@CNNs composites and CNNs were lower than the self-corrosion potential of 316 SS (−0.18 V vs. SCE), which may be due to the fact that the electrons in ZIS@CNNs composites and CNNs did not disappear completely after the light was turned off. There are still some electrons are transferred from three different ZIS@CNNs composites and CNNs photoanodes to 316 SS surface, indicating that they still played a continuous protective role for 316 SS in the dark state. In addition, three different ZIS@CNNs composites rebounded to more negative potential values compared with pure CNNs, indicating that the composite had a better continuous protection effect than pure CNNs in the dark state. The potentials of three different ZIS@CNNs composites remained stable after four on-off photocycles, indicating that the composites can provide stable protection to 316 SS for a long time. In addition, to test the protection effect of the composite material on other metals, we conducted OCP tests on 304 SS under the same conditions as 316 SS, and the potential drop compared to 316 SS was shown in the Figure 9e. It can be clearly seen that ZIS@CNNs composites have obvious protection for 304 SS, and 30% ZIS@CNNs composite has much better protection effect for 304 than CNNs. In addition, in comparison with the protection of CNNs and 30% ZIS@CNNs composite for 316 SS, the protection for 304 SS is weaker than 316 SS.

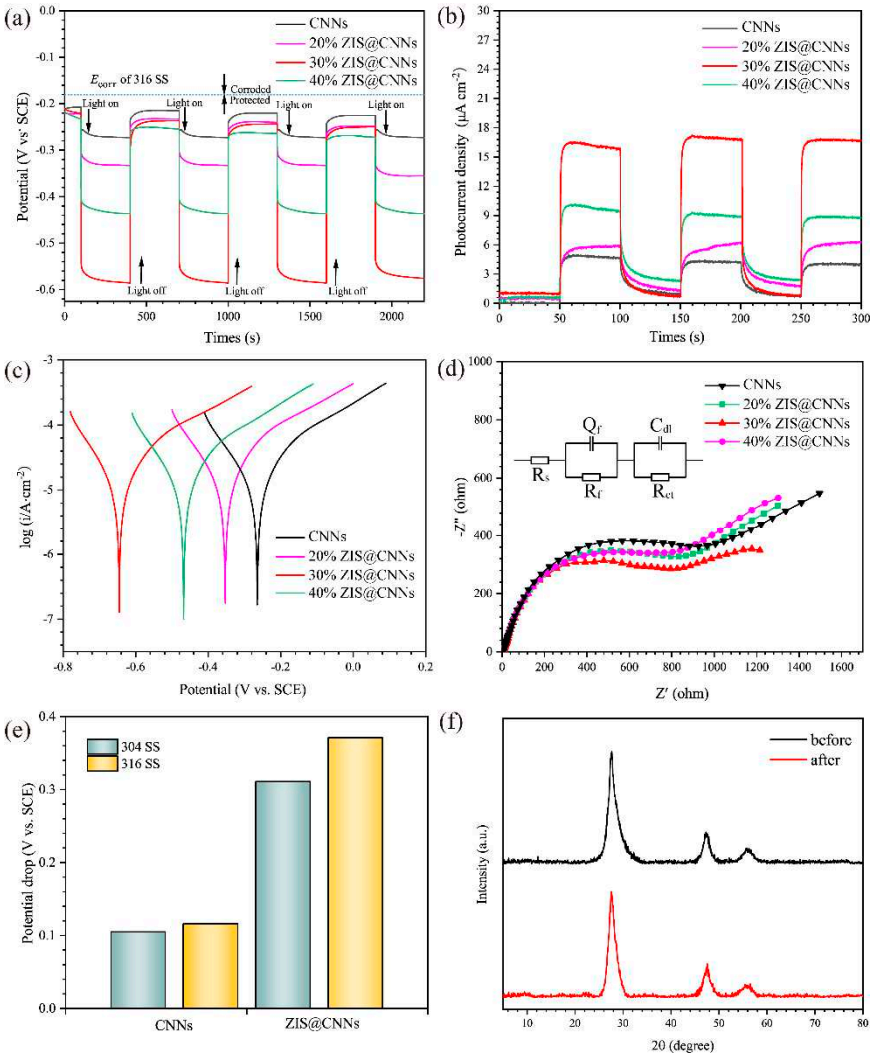

Figure 9. (a) OCP-t curves, (b) The I-t curves, (c) Tafel curves, and (d) Nyquist plots of 316 SS coupled with CNNs and three different ZIS@CNNs composites. (f) Different potential drops of 304 SS and 316

Preprints (www.preprints.org) | NOT PEER-REVIEWED | Posted: 5 July 2023 doi:10.20944/preprints202307.0233.v1

SS coupled with CNNs and ZIS@CNNs, respectively. (f) XRD patterns of 30% ZIS@CNNs composite before and after the electrochemical test.

CV curves were used to analyze the electrochemical activity of pure CNNs and three different ZIS@CNNs composites. The CV curves of four materials were tested at different sweep speeds and the results were shown in Figure 10 a-d. It can be seen from Figure 10 that the area enclosed by the CV curves of the three ZIS@CNNs composites was larger than that of the CNNs at the same sweep speed, and the area enclosed by the CV curves of the 30% ZIS@CNNs composite was the largest. The scatter plot of Figure 10e was obtained with the sweep speed as the horizontal coordinate and the current variation of the CV curve as the vertical coordinate. The data were fitted to obtain four straight lines with different slopes, and the slope allows us to obtain the capacitance values of different materials. The larger the slope, the larger the capacitance value [58]. Besides, the electrochemical active area correlated with the size of the capacitance value, the larger the capacitance value, the larger the active area. Therefore, the slope size of the 4 lines in Figure 10e could be used to qualitatively analyze the effect of the size of the electrochemically active area of the 4 materials on the protection performance of the materials. It could be seen from Figure 10e that the slopes of the three different ZIS@CNNs composites were significantly larger than that of CNNs and the slope of the 30% ZIS@CNNs composite was the largest, which indicates that the capacitance value of the three different ZIS@CNNs composites were larger than that of CNNs and the 30% ZIS@CNNs composite had the largest capacitance. Therefore, the electrochemically active areas of three different composites were greater than that of CNNs. 30% ZIS@CNNs composite had the largest electrochemically active area. This is in agreement with the 30% ZIS@CNNs composites exhibiting the optimal protective properties. In addition, the slope of the 40% ZIS@CNNs composite was slightly smaller than that of the 20% ZIS@CNNs composite, which may be attributed to the increase in the proportion of ZIS, which caused a large amount of ZIS to accumulate, resulting in smaller gaps between the nano-leaves, resulting in a reduced active area. However, more heterojunction channels were formed between the ZIS and CNNs in the 40% ZIS@ CNNs composites, which allowed the 40% ZIS@ CNNs composites to exhibit better protective properties than the 20% ZIS@CNNs composites.

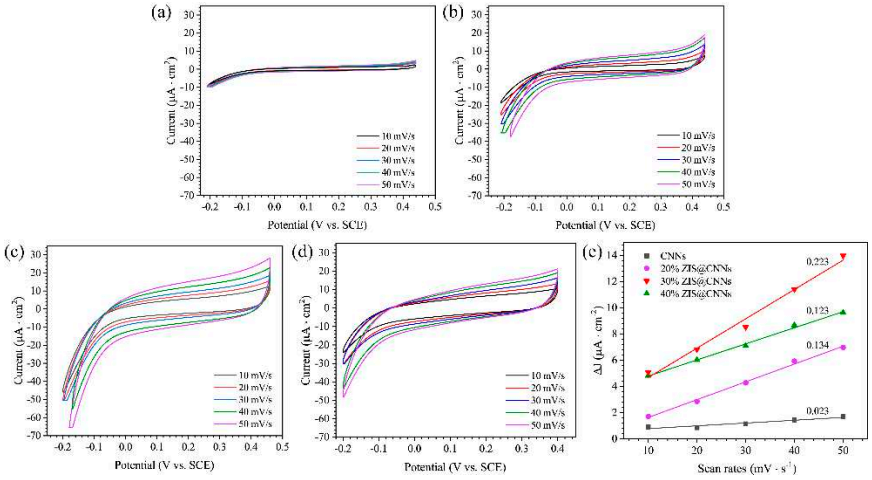

Figure 10. CV curves of (a) CNNs, (b) 20% ZIS@CNNs, and (c) 30% ZIS@CNNs (d) 40% ZIS@CNNs composite (e) Plots of the current densities of the CV curves under different scanning speeds.

The photoanodes generates current under light, therefore, photocurrent density is another effective approach to characterize the protection effect of photoanodes on 316 SS [59]. The i-t curves of 316 SS coupled with CNNs and three different ZIS@CNNs composites were measured. As shown in Figure 9b, when the light source was turned on, the photocurrent densities of all materials increased rapidly to a certain value. It was obvious from Figure 9b that the photocurrent densities of three different ZIS@CNNs composites were larger than that of pure CNNs, and 30% of ZIS@CNNs composites exhibited the largest photocurrent densities (17.30 μA cm^{-2}), which was more than 4 times that of pure CNNs (4.22 μA cm^{-2}). The current drops in the 100 ~ 150 s and 200 ~ 250 s closed-light

Preprints (www.preprints.org) | NOT PEER-REVIEWED | Posted: 5 July 2023 doi:10.20944/preprints202307.0233.v1

phases for CNNs and the three different composites were not as rapid as in the open-light phase, but more slowly, and the final steady current was not zero, which may be due to the fact that the carriers generated in the open-light phase did not disappear completely. Combined with the above and OCP results, it can be indicated that three different ZIS@CNNs composites could provide better protection for 316 SS than pure CNNs under light conditions, and the 30% ZIS@CNNs composite had the best protection effect.

Figure 9c shown the Tafel curves of 316 SS coupled with CNNs and three different ZIS@CNNs composites. Table 1 shown the fitted values of the above curves. The order of E_{corr} for different materials was that 30% ZIS@CNNs composite < 40% ZIS@CNNs composite < 20% ZIS@CNNs composite < CNNs. The 30% ZIS@CNNs composite has the most negative photogenerated potential, which is consistent with the OCP results. In addition, the order of i_{corr} for different materials is that 30% ZIS@CNNs composite > 40% ZIS@CNNs composite > 20% ZIS@CNNs composite > CNNs. The i_{corr} for 30% ZIS@CNNs composite is more than 3 times that of CNNs. Larger i_{corr} means faster electrode reaction rates [60]. i_{corr} for 30% ZIS@CNNs is the largest, indicating this composite has the highest protection efficiency.

Table 1. Fitting values of E_{corr} and i_{corr} obtained from the Figure 9c.

Samples	E_{corr} (V vs. SCE)	i_{corr} (μA cm^{-2})
CNNs	−0.271	4.08
20% ZIS@CNNs	−0.332	6.46
30% ZIS@CNNs	−0.62	13.54
40% ZIS@CNNs	−0.434	10.93

In order to study the electron transfer efficiency inside and between materials, we measured the EIS plots of 316 SS coupled with CNNs and three different ZIS@CNNs composites, and the results are shown in Figure 9d. It could be clearly seen that the impedance arcs of three different ZIS@CNNs composites were smaller than that of CNNs under the light condition, and 30% ZIS@CNNs composite has the smallest impedance arc. This indicates that the ZIS@CNNs composites generate more photogenerated electrons and the formation of heterojunction channels accelerates the electron transfer, which enhances the protection of the material for 316 SS. According to the measured impedance data, the fitted circuit used is R_s (Q_f R_f) (C_{dl} R_{ct}) circuit. The fitting circuit diagram was shown in the internal diagram of Figure 9d. R_f, R_s, and R_{ct} were the internal resistance of the photoanode, the resistance of 3.5 wt% NaCl solution, and the charge transfer resistance, respectively. Q_f and C_{dl} were defined as internal film capacitance of the material and double-layer capacitance, respectively. Table 2 shown the values of the fitting. The smaller the R_{ct}, the easier the charge transfer [61]. The order of R_{ct} of different materials was that 30% ZIS@CNNs (426.5 Ω cm^{-2}) < 40% ZIS@CNNs (556.6 Ω cm^{-2}) < 20% ZIS@CNNs (874.2 Ω cm^{-2}) < CNNs (934.1 Ω cm^{-2}). It is obviously that the R_{ct} of CNNs was about 2 times than that of 30% ZIS@CNNs composite, which means that the transfer efficiency of electrons in 30% ZIS@CNNs composite is higher than that in pure CNNs. Furthermore, 30% ZIS@CNNs composite has the highest electron transfer efficiency.

Table 2. Fitting values of EIS data.

	R_s (Ω cm^{-2})	Q_f (F·cm^{-2}·10^{-2})	R_f (Ω cm^{-2})	C_{dl} (F·cm^{-2}·10^{-2})	R_{ct} (Ω cm^{-2})
CNNs	4.605	5.411×10^{-2}	948.7	0.01807	934.1
20% ZIS@ CNNs	4.574	4.983×10^{-2}	976.3	0.02	874.2
30% ZIS@ CNNs	4.278	1.803×10^{-3}	1590	3.916×10^{-4}	426.5
40% ZIS@ CNNs	2.709	4.235×10^{-3}	1135.3	2.721×10^{-4}	556.6

The stability of the material is an important factor that affects the practical application of the material. Figure 9f shows the XRD patterns of the material before and after the electrochemical test,

Preprints (www.preprints.org) | NOT PEER-REVIEWED | Posted: 5 July 2023 doi:10.20944/preprints202307.0233.v1

and it can be seen from the figure that the XRD patterns before and after the reaction are not significantly changed. This indicates that the photoanode material has good stability.

3.4. Mechanism analysis

To determine the band edge positions of different materials and the VB and CB positions of CNNs and ZIS, and to elucidate the mechanism of electron transfer. The M-S curves of the five materials were measured. It could be seen from Figure 11 that the slopes of all the curves are positive, which indicates that the experimentally prepared ZIS, CNNs, and the three different ZIS@CNNs composites are n-type semiconductors [62]. Compared with CNNs, the flat-band potentials (E_{fb}) of composites have a negative shift, and 30% ZIS@CNNs composite has the most negative shift. It indicates that more photogenerated electrons can be transferred from the 30% ZIS@CNNs composite to the 316 SS surface for their protection than the other materials. It could be seen from Figure 12 that the E_{fb} of CNNs was –0.6 V vs. SCE, and E_{CB} could be calculated by the following formulae:

$$E_{fb}(\text{vs. NHE}) = E_{fb}(\text{vs. SCE}) - 0.24 \quad (2)$$

$$E_{CB} = E_{fb}(\text{vs. NHE}) + 0.20 \quad (3)$$

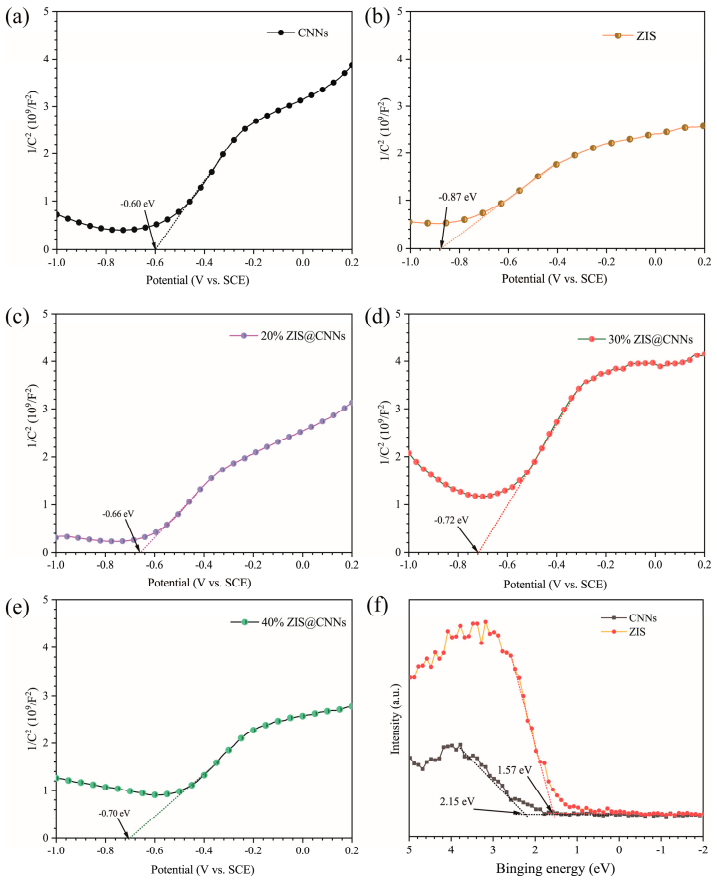

Figure 11. (a)-(e) M-S curves of CNNs, ZIS, and ZIS@CNNs composites, (f) Valence band XPS (VB XPS) spectra of CNNs and ZIS.

Preprints (www.preprints.org) | NOT PEER-REVIEWED | Posted: 5 July 2023 doi:10.20944/preprints202307.0233.v1

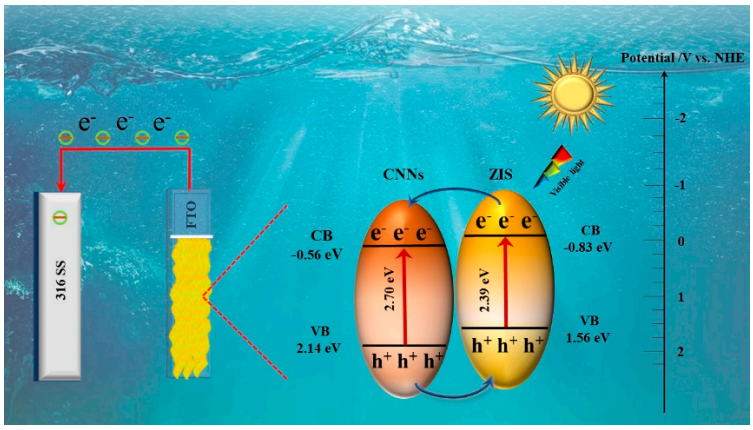

Figure 12. Electron-hole pair migration mechanism of ZIS@CNNs composite.

so the E_{CB} of CNNs is −0.56 eV. Similarly, the E_{CB} of ZIS is −0.83 eV [63,64]. E_{VB} of the semiconductor photoanodes can be calculated by the formula:

$$E_{VB} = E_{fb} - E_{CB} \quad (4)$$

So that the EVB of CNNs and ZIS were calculated as 2.14 and 1.56 eV, respectively. Besides, to further confirm the EVB, the XPS valence band spectra were tested. It could be seen from Figure 11f that the EVB of CNNs and ZIS were 2.15 and 1.57 eV, respectively, which were consistent with the M-S results. Obviously, the ECB of ZIS was more negative than that of CNNs, so the photogenerated electrons can be transferred from ZIS to CNNs surface and move to the 316 SS surface. Therefore, the ZIS@CNNs composites generate more electrons than pure CNNs.

4. Conclusions

In summary, three different 2D/2D ZIS@CNNs composites were prepared by calcination and hydrothermal method. According to the results of SEM, TEM, and BET, the compounding of 2D CNNs and 2D ZIS leads to a large number of micropores on the surface of CNNs, resulting in a significant increase in visible light absorption efficiency and generating lots of high-speed nanochannels for charge transfer. In addition, UV-Vis DRS shows that the absorption band edges of composites have a red shift that results in an increase in the absorption of visible light by the material. Photocatalysis is a complex process of carrier generation, separation, compounding, and transfer. The result of PL shows that due to the introduction of ZIS, the separation efficiency of photogenerated carriers of ZIS@CNNs composites is greatly improved. EIS shows that photogenerated carriers could rapidly transfer from the ZIS@CNNs photoanodes to the surface of 316 SS. Therefore, the introduction of ZIS brings a significant increase in both carrier separation and transfer efficiency, which lead to the improved PCP efficiency of ZIS@CNNs nanocomposite under visible light. The photocurrent density of the 30% ZIS@CNNs composite can reach 17 μA cm^{-2} and the photogenerated potential drop to about −0.58 V, indicating the effective protection of the composite. In conclusion, 2D/2D ZIS@CNNs composite is a very friendly photoanode material to protect the metal from corrosion in the ocean environment.

Supplementary Materials: The following supporting information can be downloaded at website of this paper posted on Preprints.org.

Author Contributions: Experiment, Writing - original draft, Picture drawing, review & editing, Weitao Li.; Experiment, Zhanyuan Yang.; Resources, Yanhui Li.; Resources, Pengfei Zhang.; Writing - review & editing, Supervision, Funding acquisition, Hong Li.

Funding: This work was funded by the National Natural Science Foundation of China (No. 51801109) and the Science and Technology Support Plan for Youth Innovation of Colleges in Shandong Province (No. DC2000000891).

Data Availability Statement: The authors confirm that the data supporting the findings of this study are available within the article.

Conflicts of Interest: The authors declare no conflict of interest.

References

1. Guo, H.; Zhang, Y.; Wang, S.; Li, L.; Wang, W.; Sun, Q. In-situ generation of Bi_2S_3 to construct $WO_3/BiVO_4/Bi_2S_3$ heterojunction for photocathodic protection of 304 SS. *J Electroanal Chem*. **2022**, 907, 116033.
2. Wang, X.; Pu, J.; Liu, J.; Ren, M.; Nan, Y.; Liu, M.; Xu, H.; Yang, L.; Huang, Y.; Hou, B. PDA decorated spaced TiO_2 nanotube array photoanode material for photocathodic protection of 304 stainless steels. *J Electroanal Chem*. **2022**, 914, 116319.
3. Wang, X.; Xu, H.; Nan, Y.; Sun, X.; Duan, J.; Huang, Y.; Hou, B. Research progress of TiO_2 photocathodic protection to metals in marine environment. *J Oceanol Limnol*, **2020**, 38, 1018-1044.
4. Zhang, J.; Yang, H.; Wang, Y.; Cui, X.; Wen, Z.; Liu, Y.; Fan, L.; Feng, J. Facile fabrication of SnO2 modified TiO_2 nanorods film for efficient photocathodic protection of 304 stainless steel under simulated solar light. *Corros Sci*. **2020**, 176, 108927.
5. Qiu, J.; Wei, S.; Pan, J.; Liang, Z.; Ma, J.; Liang, Q.; Li, C. g-C_3N_4-loaded carbon nanofiber for efficient photocatalytic hydrogen production. *Integr Ferroelectr*. **2023**, 231, 70-77.
6. Zhang, X.; Liang, H.; Li, C.; Bai, J. 1D CeO_2/g-C_3N_4 type II heterojunction for visible-light-driven photocatalytic hydrogen evolution. *Inorg Chem Commun*, **2022**, 144, 109838.
7. Ren, T.; Dang, Y.; Xiao, Y.; Hu, Q.; Deng, D.; Chen, J.; He, P. Depositing Ag nanoparticles on g-C_3N_4 by facile silver mirror reaction for enhanced photocatalytic hydrogen production, *Inorg Chem Commun*, **2021**, 123, 108367.
8. Li, X.; Liu, T.; Tian, F.; Tao, X.; Wu, Z.S. Enhanced carrier transport and visible light response in CA-β-CD/g-C_3N_4/Ag_2O 2D/0D heterostructures functionalized with cyclodextrin for effective organic degradation. *Korean J Chem Eng*, **2022**, 39, 2972-2982.
9. [9]. Yu, X.; Zhang, X.; Zhao, J.; Xu, L.; Yan, J. Flower-like shaped $Bi_{12}TiO_{20}$/g-C_3N_4 heterojunction for effective elimination of organic pollutants: preparation, characterization, and mechanism study. *Appl Organomet Chem*. **2020**, 34, 0268-2605.
10. Mao, N.; Jiao, Y.; Duan, X. g-C_3N_4/ZnO heterojunction as Fenton-like catalyst for degradation of organic pollution. *Mater Res Bull*, **2022**, 151, 111818.
11. Zhu, X.; Deng, H.; Cheng, G. Facile construction of g-C_3N_4-$W_{18}O_{49}$ heterojunction with improved charge transfer for solar-driven CO_2 photoreduction. *Inorg Chem Commun*. **2021**, 132, 108814.
12. Huang, M.; Chen, C.; Wang, T.; Sui, Q.; Zhang, K.; Li, B. Cadmium-sulfide/gold/graphitic-carbon-nitride sandwich heterojunction photocatalyst with regulated electron transfer for boosting carbon-dioxide reduction to hydrocarbon. *J Colloid Interf Sci*. **2022,** 613, 575-586.
13. Zhang, R.; Cao, Y.; Doronkin, D.; Ma, M.; Dong, F.; Zhou, Y. Single-atom dispersed Zn-N_3 active sites bridging the interlayer of g-C_3N_4 to tune NO oxidation pathway for the inhibition of toxic by-product generation. *Chem Eng J*, **2023**, 454, 140084.
14. Liang, Y.; Zeng, Z.; Yang, J.; Yang, G.; Han, Y. Designing heterointerface in BiOBr/ g-C_3N_4 photocatalyst to enhance visible-light-driven photocatalytic performance in water purification. *Colloid Surface A*, **2021**, 624, 126796.
15. Ni, Y.; Wang, M.; Liu, L.; Li, M.; Hu, S.; Lin, J.; Sun, J.; Yue, T.; Zhu, M.; Wang, J. Efficient and reusable photocatalytic river water disinfection by addictive graphitic carbon nitride/magnesium oxide nano-onions with particular "nano-magnifying glass effect". *J Hazard Mater*, **2022**, 439, 129533.
16. Rao, F.; Zhong, J.; Li, J. Improved visible light responsive photocatalytic hydrogen production over g-C_3N_4 with rich carbon vacancies. *Ceram Int*, **2022**, 48, 1439-1445.
17. Shi, Z.; Rao, L.; Wang, P.; Zhang, L. The photocatalytic activity and purification performance of g-C_3N_4/carbon nanotubes composite photocatalyst in underwater environment. *Environ Sci Pollut R*, **2022**, 29, 83981-83992.
18. Cao, J.; Cai, J.; Li, R.; Han, J.; Liu, J.; Huang, M. A novel 3D yolk-double-shell Au@CdS/ g-C_3N_4 nanostructure with enhanced photoelectrochemical and photocatalytic properties. *J Phys Chem C*, **2022**, 126, 4939-4947.
19. Saeidpour, S.; Khoshnevisan, B.; Boroumand, Z. Synthesis and characterization of a g-C_3N_4/TiO_2-ZnO nanostructure for photocatalytic degradation of methylene blue. *Nano Futures*, **2022**, 6, 035001.

20. Liu, F.; Bi, S.; Wang, W.; Duan, Q.; Feng, Y.; Chen, J.; Luo, R.; Huang, Y.; Lee, J. Preparation of a modified g-C_3N_4 catalyst library and realization of a two-dimensional screening reaction. *New J Chem*, **2021**, 45, 2582-2588.
21. Deng, L.; Sun, J.; Sun, J.; Wang, X.; Shen, T.; Zhao, R.; Zhang, Y.; Wang, B. Improved performance of photosynthetic H_2O_2 and photodegradation by K-, P-, O-, and S-co-doped g-C_3N_4 with enhanced charge transfer ability under visible light. *Appl Surf Sci*, **2022**, 597, 153586.
22. Ge, Y.; Guo, X.; Zhou, D.; Liu, J. Construction and excellent photoelectric synergistic anticorrosion performance of Z-scheme carbon nitride/tungsten oxide heterojunctions. *Nanoscale*, **2022**, 14, 12358-12376.
23. Zhou, W.; Lu, S.; Chen, X. Anionic donor-acceptor conjugated polymer dots/g-C_3N_4 nanosheets heterojunction: High efficiency and excellent stability for co-catalyst-free photocatalytic hydrogen evolution. *J Colloid Interf Sci*. **2022**, 608, 912-921.
24. Yan, X.; Xie, M.; Pan, L.; Ai, T.; Li, Z.; Niu, Y. Piezo-photocatalytic activity of $NaNbO_3$/g-C_3N_4 heterojunction for dye wastewater degradation. *Journal of Materials Science: Materials in Electronics*, **2023**, 34, 0957-4522.
25. Vavilapalli, D.; Peri, R.; B, M.; Sridharan, K.; Rao, M.; Singh, S. Enhanced photocatalytic and photoelectrochemical performance of $KBiFe_2O_5$/g-C_3N_4 heterojunction photocatalyst under visible light. *Physica B: Condensed Matter*, **2023**, 648, 414411.
26. Huang, Y.; Li, B.; Wu, F.; Yang, B. Fabrication of novel flower-like Co_3O_4/g-C_3N_4 heterojunction for tetracycline degradation under visible light irradiation. *Materials Letters*, **2022**, 311, 131538.
27. Wang, Z.; Zhang, J.; Ji, X.; Wu, H.; Xu, X.; Zhan, J.; Shi, H.; Liu, W.; Tang, T. Construction of CdSe/$ZnIn_2S_4$ Z-Scheme heterojunction for enhanced photocatalytic degradation of tetracycline. *Mater Sci Eng B-Adv*, **2022**, 286, 116065.
28. Yang, N.; Li, J. Construction of a 0D/2D heterojunction based on ZnO nanoparticles and $ZnIn_2S_4$ nanosheets to improve photocatalytic degradation efficiency. *Opt Mater*, **2021**, 115, 111040.
29. Wang, Z.; Su, B.; Xu, J.; Hou, Y.; Ding, Z. Direct Z-scheme $ZnIn_2S_4$/$LaNiO_3$ nanohybrid with enhanced photocatalytic performance for H_2 evolution. *Int J Hydrogen Energ*, **2020**, 45, 4113-4121.
30. Zhu, J.; Li, H.; Cui, X.; Yang, Z.; Chen, B.; Li, Y.; Zhang, P.; Li, J. Efficient photocathodic protection performance of $ZnIn_2S_4$ nanosheets/SnO_2 quantum dots/TiO_2 nanotubes composite for 316 SS under visible light. *J Alloy Compd*, **2022**, 926, 166901.
31. Cao, S.; Yu, J.; Wageh, S.; Al-Ghamdi, A.; Mousavi, M.; Ghasemi, J.; Xu, F. H_2-production and electron-transfer mechanism of a noble-metal-free WO_3@$ZnIn_2S_4$ S-scheme heterojunction photocatalyst. *Journal of Materials Chemistry A*, **2022**, 10, 17174-17184.
32. Wang, K.; Shao, X.; Cheng, Q.; Li, K.; Le, X.; Wang, G.; Wang, H. In situ-Illuminated X-Ray photoelectron spectroscopy investigation of S-scheme Ta_2O_5/$ZnIn_2S_4$ core-shell hybrid nanofibers for highly efficient solar-driven CO_2 overall splitting. *Solar Rrl*, **2022**, 6, 2367-198X.
33. Zhang, L.; Qiu, J.; Dai, D.; Zhou, Y.; Liu, X.; Yao, J. Cr-metal-organic framework coordination with $ZnIn_2S_4$ nanosheets for photocatalytic reduction of Cr(VI). *Journal of Cleaner Production*, **2022**, 341, 130891.
34. Dang, X.; Xie, M.; Dai, F.; Guo, J.; Liu, J.; Lu, X. Ultrathin 2D/2D $ZnIn_2S_4$/g-C_3N_4 nanosheet heterojunction with atomic-level intimate interface for photocatalytic hydrogen evolution under visible light. *Adv Mater Interfaces*, **2021**, 8, 2196-7350.
35. Hou, L.; Li, W.; Wu, Z.; Wei, Q.; Yang, H.; Jiang, Y.; Wang, T.; Wang, Y.; He, Q. Embedding ZnCdS@$ZnIn_2S_4$ into thiazole-modified g-C_3N_4 by electrostatic self-assembly to build dual Z-scheme heterojunction with spatially separated active centers for photocatalytic H_2 evolution and ofloxacin degradation. *Separation and Purification Technology*, **2022**, 290, 120858.
36. Li, Y.; Lu, Y.; Wang, Y.; Dong, L.; Chao, M.; Sun, J.; Zhao, Z.; Zhang, J. One-step synthesis of high photocatalytic graphitic carbon nitride porous nanosheets. *Nanotechnology*, **2020**, 31, 0957-4484.
37. Ai, L.; Fan, H. CTAB-melamine molecular crystals as precursor for synthesis of layered carbon nitride porous nanostructures with enhanced photocatalytic activity for hydrogen production. *Mater Today Commun*, **2021**, 29, 102780.
38. Zhu, K.; Luan, X.; Matras-Postolek, K.; Yang, P. 2D/2D MoS_2/g-C_3N_4 layered heterojunctions with enhanced interfacial electron coupling effect. *J Electroanal Chem*, **2021**, 893, 115350.
39. Kesir, M.; Yildiz, I.; Bilgen, S.; Sokmen, M. Role of a novel cationic gemini surfactant (CGS) on a one-step sol-gel process and photocatalytic properties of TiO_2 powders. *J Water Health*, **2022**, 20, 1629-1643.

40. Wang, X.; Chen, X.; Thomas, A.; Fu, X.; Antonietti, M. Metal-containing carbon nitride compounds: A new functional organic-metal hybrid material. *Adv Mater*, **2009**, 21, 1609-+.
41. Wang, X.; Maeda, K.; Thomas, A.; Takanabe, K.; Xin, G.; Carlsson, J.; Domen, K.; Antonietti, M. A metal-free polymeric photocatalyst for hydrogen production from water under visible light, *Nature Materials*, **2009**, 8, 76-80.
42. Jo, W.; Natarajan, T. Influence of TiO_2 morphology on the photocatalytic efficiency of direct Z-scheme g-C_3N_4/TiO_2 photocatalysts for isoniazid degradation. *Chem Eng J*, **2015**, 281, 549-565.
43. Guo, F.; Huang, X.; Chen, Z.; Cao, L.; Cheng, X.; Chen, L.; Shi, W. Construction of Cu_3P-$ZnSnO_3$-g-C_3N_4 p-n-n heterojunction with multiple built-in electric fields for effectively boosting visible-light photocatalytic degradation of broad-spectrum antibiotics. *Sep Purif Technol*, **2021**, 265, 118477.
44. Zhang, W.; Shi, W.; Sun, H.; Shi, Y.; Luo, H.; Jing, S.; Fan, Y.; Guo, F.; Lu, C. Fabrication of ternary CoO/g-C_3N_4/Co_3O_4 nanocomposite with p-n-p type heterojunction for boosted visible-light photocatalytic performance. *J Chem Technol Biot*, **2021**, 96, 1854-1863.
45. Ni, T.; Yang, Z.; Cao, Y.; Lv, H.; Liu, Y. Rational design of MoS_2/g-C_3N_4/$ZnIn_2S_4$ hierarchical heterostructures with efficient charge transfer for significantly enhanced photocatalytic H_2 production. *Ceram Int*, **2021**, 47, 22985-22993.
46. Ye, X.; Zhu, T.; Hui, Z.; Wang, X.; Wei, J.; Chen, S. Revealing the transfer mechanisms of photogenerated charge carriers over g-C_3N_4/$ZnIn_2S_4$ composite: A model study for photocatalytic oxidation of aromatic alcohols with visible light. *J Catal*, **2021**, 401, 149-159.
47. Fu, D.; Han, G.; Liu, F.; Xiao, Y.; Wang, H.; Liu, R.; Liu, C. Visible-light enhancement of methylene blue photodegradation by graphitic carbon nitride-titania composites. *Materials Science in Semiconductor Processing*, **2014**, 27, 966-974.
48. Wang, F.; Zhao, Y.; Zhang, M.; Wu, J.; Liu, G.; He, P.; Qi, Y.; Li, X.; Zhou, Y.; Li, J. Bimetallic sulfides $ZnIn_2S_4$ modified g-C_3N_4 adsorbent with wide temperature range for rapid elemental mercury uptake from coal-fired flue gas, *Chem Eng J*, **2021**, 426, 131343.
49. Yang, L.; Zhao, J.; Wang, Z.; Wang, L.; Zhao, Z.; Li, S.; Li, G.; Cai, Z. Facile construction of g-C_3N_4/$ZnIn_2S_4$ nanocomposites for enhance Cr(VI) photocatalytic reduction. *Spectrochim Acta A*, **2022**, 276, 121184.
50. Zheng, H.; Liu, Y.; Zhou, Y.; Zhao, D.; Wang, D.; Yun, L.; Zhang, D.; Zhang, L. Improved photocathodic protection performance of g-C_3N_4/rGO/ZnS for 304 stainless steel. *J Phys Chem Solids*, **2021**, 148, 109672.
51. Mishra, N.; Kuila, A.; Saravanan, P.; Bahnemann, D.; Jang, M.; Routu, S. Simultaneous S-scheme promoted Ag@$AgVO_3$/g-C_3N_4/$CeVO_4$ heterojunction with enhanced charge separation and photo redox ability towards solar photocatalysis. *Chemosphere*, **2023**, 326, 138496.
52. Rajendran, R.; Vignesh, S.; Sasireka, A.; Priya, P.; Suganthi, S.; Raj, V.; Sundar, J.K.; Srinivasan, M.; Shkir, M.; AlFaify, S. Investigation on novel Cu_2O modified g-C_3N_4/ZnO heterostructures for efficient photocatalytic dye degradation performance under visible-light exposure. *Colloid Interfac Sci*. **2021**, 44, 100480.
53. Wu, B.; Shan, C.; Zhang, X.; Zhao, H.; Ma, S.; Shi, Y.; Yang, J.; Bai, H.; Liu, Q. CeO_2/Co_3O_4 porous nanosheet prepared using rose petal as biotemplate for photo-catalytic degradation of organic contaminants. *Appl Surf Sci*. **2021**, 543, 148677.
54. Sivanandan, V.; Prasad, A. Lactose monohydrate ($C_{12}H_{22}O_{11}$ center dot H_2O) mediated synthesis and spectral analysis of nanocrystalline $Ni_{0.5}Cu_{0.5}Fe_2O_4$. *International Journal of Materials Research*, **2021**, 112, 980-984.
55. Huang, X.; Xu, X.; Yang, R.; Fu, X. Synergetic adsorption and photocatalysis performance of g-C_3N_4/Ce-doped MgAl-LDH in degradation of organic dye under LED visible light, *Colloid Surface A*. **2022**, 643, 128738.
56. Hoang, T.; Nguyen, P.; Shin, E. Effect of morphological modification over g-C_3N_4 on photocatalytic hydrogen evolution performance of g-C_3N_4-Pt photocatalysts, *Catalysts*, **2023**, 13, 10092.
57. Zhang, T.; Liu, Y.; Liang, J.; Wang, D. Enhancement of photoelectrochemical and photocathodic protection properties of TiO_2 nanotube arrays by simple surface UV treatment. *Appl Surf Sci*. **2017**, 394, 440-445.
58. Tian, J.; Chen, Z.; Ma, L.; Hou, J.; Feng, C.; Jing, J.; Sun, M.; Chen, D. Fabrication of flower-like WO_3/$ZnIn_2S_4$ composite with special electronic transmission channels to improve carrier separation for photoinduced cathodic protection and electron storage. *Appl Surf Sci*. **2023**, 607, 155019.
59. Gong, D.; Xu, S.; Zhang, K.; Du, L.; Qiu, P. Enhancing photoelectrochemical cathodic protection performance by facile tuning sulfur redox state in sacrificial agents. *Chem Eng J*, **2023**, 451, 138552.

60. Yang, Z.; Li, H.; Cui, X.; Zhu, J.; Li, Y.; Zhang, P.; Li, J. Direct Z-scheme nanoporous $BiVO_4$/CdS quantum dots heterojunction composites as photoanodes for photocathodic protection of 316 stainless steel under visible light. *Appl Surf Sci*. **2022**, 603, 154394.
61. Kathiravan, S.; Kaliaraj, G.; Kumar, R.; Kirubaharan, A. A novel experimental setup for in situ oxidation behavior study of Nb/Hf/Ti (C-103) alloy for high temperature environments. *Materials Letters*, **2021**, 302, 130336.
62. Igbari, F.; Essien, E; Abdulwahab, K.; Nejo, A.; Adetona, A.; Adams, L.A. Bipolar conductivity in amorphous Cu-Al-O thin films prepared by r.f. magnetron sputtering. *Materials Science in Semiconductor Processing*, **2021**, 123, 105557.
63. Duan, Z.; Zhao, X.; Chen, L. $BiVO_4$/$Cu_{0.4}V_2O_5$ composites as a novel Z-scheme photocatalyst for visible-light-driven CO_2 conversion. *J Environ Chem Eng*, **2021**, 9, 104628.
64. Wang, W.; Feng, X.; Chen, L.; Zhang, F. Z-Scheme Cu_2O/Bi/$BiVO_4$ nanocomposite photocatalysts: synthesis, characterization, and application for CO_2 photoreduction. *Ind Eng Chem Res*, **2021**, 60, 18384-18396.